System-Technology Co-Optimization of Multimetal Gated AlGaN/GaN HEMT for Improved RF Linearity

Toiyob Hossain, Tanvir Hossain, A. K. M. Anindya Alam, Bejoy Sikder, Qingyun Xie, Mengyang Yuan, Eiji Yagyu, Koon Hoo Teo, Tomás Palacios, *Fellow, IEEE*, and Nadim Chowdhury, *Senior Member, IEEE*

***Abstract*—In this work, a system-technology co-optimization (STCO) of the AlGaN/GaN multimetal gated (MMG) HEMT architecture for third-order transconductance *(g_{m3})* engineering and linearity improvement in the presence of fermi-level pinning (FLP) is reported. Through technology computer-aided design (TCAD), compact modeling, load-pull simulations and modulated signal simulations, it is shown that despite incorporating FLP, employing MMG scheme improves device level g_{m3} - suppression, leading to an improvement in output-referred third-order intercept point per unit dc power *($OIP3/P_{DC}$)* and third order intermodulation distortion *(IMD3)*. Remarkably, $OIP3/P_{DC}$ of 18.9 dB is obtained considering an FLP factor of 0.43, which is a 10.7 dB improvement over the conventional HEMT. MMG HEMT exhibits an output-referred 1-dB compression point *($P_{1\text{-}dB}$)* of 3.60 W/mm, compared to 0.60 W/mm for the standard/conventional case. A comparative analysis on output power back-off (OBO) for conventional and MMG HEMT with different FLP factors establishes MMG as a robust architecture to FLP. Simulations involving 5G FR1 signals demonstrate that the adjacent channel power ratio (ACPR) is sustained below −40 dBc up to an output power of 20 dBm. 2.6% lower error vector magnitude (EVM) than baseline case is achieved by MMG HEMT at 5 GHz, under 100 MHz 64-QAM OFDM signals.**

***Index Terms*—5G, Linearity, AlGaN/GaN, High Electron Mobility Transistor (HEMT), Multi-Metal Gate (MMG), Fermi Level Pinning, $OIP3/P_{DC}$, EVM, ACPR.**

I. Introduction

5G and beyond technology is positioned to drive the evolution of mobile connectivity and internet of things (IoT) applications [1], [2]. This high-frequency technology facilitates the efficient operation of modern mobile base stations, which necessitate high power density to transmit signals over extended distances. High-frequency and high power system-on-chip (SoC) devices are also essential to support high-speed end-to-end communication [3]. Gallium Nitride (GaN) technology demonstrates the best-in class RF front-end performance with a superior power density and power added efficiency (PAE) combination [4]–[7] compared to what is achievable by SOI, bulk CMOS, SiGe HBT, and other III-V HEMT/HBT technologies [8].

To reduce adjacent channel interference in the heavily packed 5G frequency bands, power amplifiers (PA) used in base stations must be highly linear, posing a substantial challenge for GaN HEMTs [9]. Furthermore, 5G communication involves high uplink and downlink transmission speeds, necessitating the use of higher-order modulation methods [10], [11]. Consequently, to maintain stringent linearity requirements, the PAs are required to operate at high peak-to-average power ratio (PAPR) and output power back-off (OBO), limiting the RF front-end performance.

Recent device-level works to achieve a linear PA include epitaxial modification such as PolFET [12], [13], graded channel HEMT [14], [15], closely coupled channel [16] HEMTs etc. Architectural modification such as variable fin width [17], multimetal gated HEMT [18], selective area charge implantation [19], buried gate [20], transitional recessed gate [21] have also been proposed. Of the various factors at the device-level that contribute to the nonlinearity of a signal in a PA, it is the third-order transconductance *(g_{m3})* that exerts the most significant influence (48% contribution) [22]. Threshold voltage (V_{TH}) engineering is an effective technique for the reduction of g_{m3}, and hence, the improvement of system-level linearity performance [23].

Azad *et al.* [18] proposed Multimetal gated (MMG) HEMT that employs threshold modulation technique using multiple metals as gate material along the width of the device. A 6.3 dB improvement in OIP_3/P_{DC} was achieved in the GaN HEMT PA after reducing the third-order transconductance *(g_{m3})* of the device by a factor of 3. Third-order transconductance *(g_{m3})* is defined as

$$g_{m3} = \frac{d^3 I_{DS}}{dV_{GS}^3} \tag{1}$$

The MMG HEMT achieves V_{TH} modulation by employing metals with different metal work-function. These metals form varied Schottky barrier height (SBH) at the metal/AlGaN

This work was supported in part by Bangladesh University of Engineering and Technology, in part by Information and Communications Technology Division, Government of Bangladesh, and in part by Mitsubishi Electric Research Labs. *(Corresponding author: N. Chowdhury)*

To. Hossain, Ta. Hossain, A.K.M. A. Alam, B. Sikder and N. Chowdhury are with the Department of Electrical and Electronic Engineering, Bangladesh University of Engineering and Technology, Dhaka-1205, Bangladesh (e-mail: {0423062384, 1906040, 1906065, bejoy, nadim} @eee.buet.ac.bd)

Q. Xie, and T. Palacios are with Microsystems Technology Laboratories, Massachusetts Institute of Technology, Cambridge, MA 02139, U.S.A. (e-mail: {qyxie, tpalacios} @mit.edu)

M. Yuan was with Microsystems Technology Laboratories, Massachusetts Institute of Technology, Cambridge, MA 02139, U.S.A. He is presently with Apple Inc., Cupertino, CA 95014, U.S.A. (e-mail: myyuan@alum.mit.edu)

Eiji Yagyu is with Mitsubishi Electric Corporation, Advanced Technology R&D Center, 8-1-1, Tsukaguchi-honmachi, Amagasaki City 661-8661, Japan. (e-mail: yagyu.eiji@cb.mitsubishielectric.co.jp)

K. H. Teo is with Mitsubishi Electric Research Labs, Cambridge, MA 02139, U.S.A. (e-mail: teo@merl.com)

interface, which, in turn, produces transistors with distinct threshold voltages in a single device.

The threshold voltage is related to the SBH by the following equation:

$$V_{TH} = \phi_B - \frac{\Delta E_C}{q} - \frac{qN_d d^2}{2\varepsilon_N} \quad (2)$$

Here, ϕ_B is the SBH, ΔE_c is the conduction band offset, q is the charge of electron, N_d is the doping concentration in barrier, d is the thickness of the barrier and ε_N is the permittivity of barrier meterial. In this context, fermi-level pinning (FLP) represents a significant issue that affects the modulation of threshold voltages. FLP depends highly on sample preparation, surface treatment, and post gate annealing [24]. However, despite several experimental reports on FLP, there is a lack of studies to understand the device performance in the presence of FLP. Such a problem becomes more pronounced in an MMG architecture. In MMG scheme, the modulation of V_{TH} was achieved by placing different metals along the width of the device. However, previous work [18] on MMG HEMT assumed an ideal Schottky behavior of the metal/AlGaN contacts without considering FLP, a first-order non-ideal effect of practical metal/semiconductor contacts.

This work, extended from a conference report [25], involves the study of seven metals for MMG architecture in the presence of FLP and provides a detailed system-technology co-optimization (STCO) of the issues that impact MMG HEMT. Specifically, two distinctive areas are explored that were not addressed before in previous work [18] : (i) modeling and detailed explanation of practical problems with MMG HEMT such as gate leakage and FLP (ii) an alternative method of gate metalization to achieve the same effect as MMG HEMT. Moreover, to verify the linearization technique, modulated signal performance (under 100 MHz 16-/64-QAM OFDM) using 5G FR1 communication standard is reported, whereas previous works [18], [19] reported upto large-signal continuous wave (CW) performances.

The organization of the article is as follows. Section II presents the device structure and simulation methodology. Section III describes the results and discussion that includes TCAD simulation, g_{m3} optimization, large-signal CW and modulated signal performance of the proposed MMG HEMT. Section IV concludes the article.

II. Device Structure and Simulation Methodology

In the schematic of the device active area, Fig. 1(a) shows M_1, M_2 and M_3, the representative metals placed along the width of the device to modulate V_{TH}. Another topology with similar effects could be using different metals in distinct fingers, as shown in Fig. 1(b) (M_1 in finger 1, M_2 in finger 2). Fundamentally, both of these technique follow the principle of parallel connected HEMTs (Fig. 1(c)), each with distinct V_{TH} to achieve a slow turn-on, and hence, lower values of the derivatives of transconductance.

The simulation framework includes experimentally calibrated TCAD models [26], g_{m3} optimization, compact modeling, large-signal CW simulation and modulated signal simulation for performance evaluation of the PA, as reported in [27], [28]. Key simulation parameters have been reported in [18].

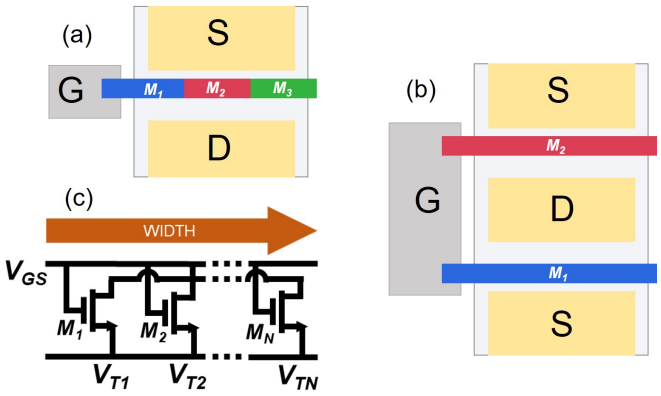

Fig. 1. (a) The top-view schematic of the device active region displays three separate gate metals across the width of a device finger. M_1, M_2, and M_3 are different metals with their numbers, widths, and work functions as optimization parameters (b) An alternative configuration for the multimetal gate involves using different metals as gate material for each finger. (c) Circuit representation of the threshold modulation technique using multimetal gate. This device imitates parallelly connected HEMTs with common gate bias.

The FLP effect has been considered in the simulation framework through the dependence of the threshold voltage of a HEMT on the SBH as given in Eq. 2. Ideally, V_{TH} modulation should be exactly 1 V for a change of 1 eV in metal work-function (ϕ_M), or in other words, a slope of 1 V/eV. However, FLP restricts the variation of SBH despite a variation in ϕ_M. In literature, in the presence of FLP, the dependence of SBH on ϕ_M is described by a slope parameter S instead of ideal slope 1 V/eV. S = 1 implies the ideal case with no pinning and S = 0 indicates that the fermi-level is pinned at a certain energy level for all metals. Reports of metal/AlGaN contacts show S values lower than 1 [29]. In this work, two values (0.43 and 0.70) of S have been investigated to quantify the effect on g_{m3} improvement (and therefore RF linearity) in MMG HEMT. S is incorporated in the simulation through the dependence of V_{TH} on ϕ_M as in Eq. 3.

$$S = \frac{\Delta\phi_B}{\Delta\phi_M} = \frac{\Delta V_{TH}}{\Delta\phi_M} < 1 \quad (3)$$

The process followed to optimize g_{m3} (minimize over a large range of V_{GS}) is often termed as "g_m compensation" [17]. g_{m3} curves of different metals were analytically superimposed. Those metals will be distributed along the width of the proposed HEMT. As a result, g_{m3} of each metal will be scaled by their sub-gate (a portion of the gate formed by a single metal) widths. The sub-gate widths $\{W_1, W_2, .., W_N\}$ are then used as the optimizing parameter in a linear mathematical function as in Eq. 4.

$$g_{m3} = W_1 \times g_{m3,M_1} + W_2 \times g_{m3,M_2} + ... + W_N \times g_{m3,M_N} \quad (4)$$

If different metals were used for different gate fingers (Fig. 1(b)), a slightly different minimization technique would be formulated, with only the metal types and work functions as optimization parameters (the gate width for each finger will be fixed). This leads to a superposition scope to minimize g_{m3}. In this work, we have studied the case where numbers of different

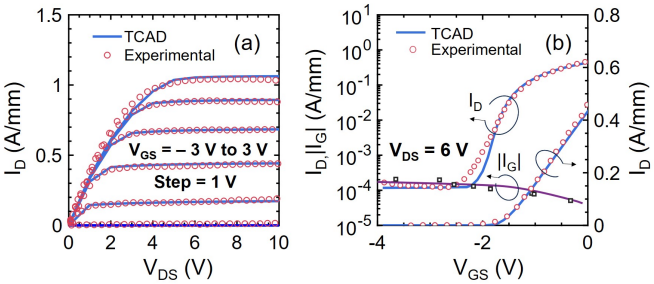

Fig. 2. Calibration of TCAD simulation models based on experimental data taken from [26]. (a) I_D-V_{DS} (b) I_D-V_{GS} and $I_G - V_{GS}$ characteristics.

gate metals used, their widths, and work-functions could be the optimization parameters (Fig. 1(a)).

III. Results and Discussion

A. TCAD Simulation

After obtaining an excellent fit between TCAD simulations and experimental data [26] (Fig. 2), the I_D–V_{GS} characteristics for seven different metals (W, Ag, Ru, Ni, Au, Ir, and Pt) have been simulated, as shown in Fig. 3(a). Seven metals with seven different work-functions ranging from 4.55 to 5.70 eV [30], [31] were chosen for this study. Gate work-function modulates the threshold voltage of the HEMT and the I_D–V_{GS} curve gets right-shifted in the V_{GS}-axis with the increase of work function, as shown in Fig. 3(a). I_D–V_{GS} curves of low work-function metals show high leakage current ($\approx 3 \times 10^{-4}$ A/mm for W), which is three orders of magnitude higher than metals with high work-functions. ($\approx 2 \times 10^{-7}$ A/mm for Pt).

Fig. 3(b) shows the variation of V_{TH} with respect to ϕ_M for different values of S. The standard deviation of threshold voltage is 0.55 V for $S = 1$, 0.38 V for $S = 0.70$ and 0.24 V for $S = 0.43$. This shift in threshold voltage eventually causes a distribution of different metals' g_{m3} curves across the V_{GS}-axis (Fig. 4(a)–(c)). It should be noted that the peak value of g_{m3} (normalized) remained the same for devices with individual metals.

B. g_{m3} Optimization

As previously mentioned, MMG HEMT achieves the lower g_{m3} through the superposition of adjacent gate-metals' g_{m3}. Therefore, V_{TH} distribution of the metals is an important factor in the degree of optimization. Fig. 4(a)–(c) depict the g_{m3} profile for different FLP factors. The resulting decrease in the standard deviation of V_{TH} leads to a narrower optimization window for g_{m3} cancellation. The metal work functions, and their gate-widths are chosen by employing the optimization technique explained in [18]. We choose Ni gated HEMT as the control case (single gated/conventional HEMT) for comparison.

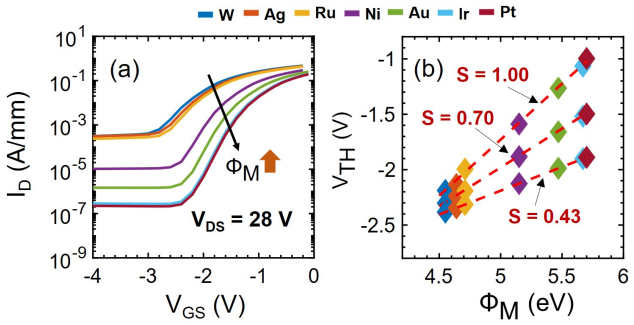

Fig. 3. (a) Simulated I_D-V_{GS} characteristics of a recessed gate AlGaN/GaN HEMT with different gate metals. (b) Threshold variation with gate-metal work-functions for different fermi-Level pinning factors, S. A linear relation is preserved even though the standard deviations of V_{TH} values decrease with decreasing S.

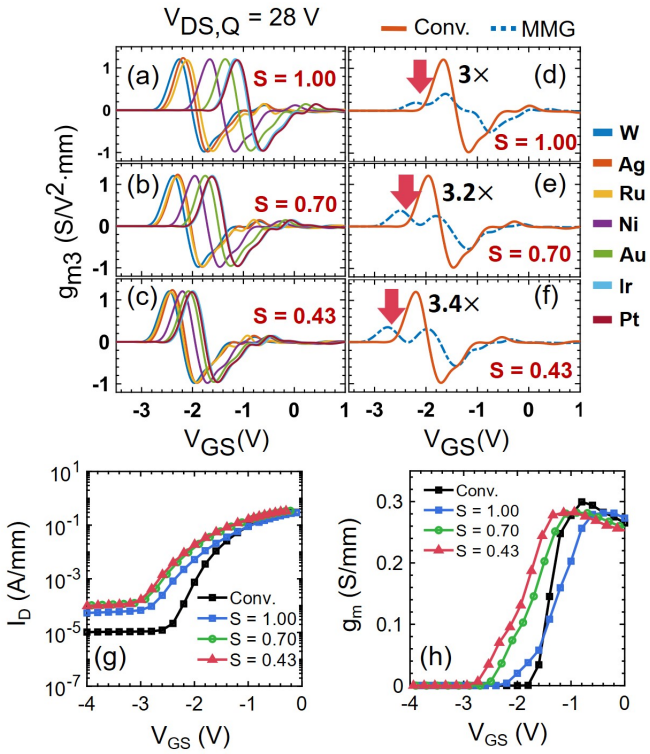

Fig. 4. (a),(b) and (c) g_{m3} peaks of different metals get closer as the pinning effect takes charge.(d), (e) and (f) Optimization of g_{m3} with an optimized selection of metals (W-10.53%, Ag-5.26%, Ni-42.11%, Au-10.53%, Ir-15.79%, Pt-15.79% for S = 1.00. W-19.5%, Ru-14.9%, Ni-30.2%, Au-35.4% for S = 0.70, and W-18.7%, Ru-13.8%, Ni-23.7% Au-43.8% for S = 0.43) as percentage of the device width considering FLP. Comparison of (g) I_D–V_{GS} and (h) g_m-V_{GS} characteristics of conventional AlGaN/GaN HEMT and proposed MMG AlGaN/GaN HEMT with an optimized selection of metals, considering three FLP factors, S.

In [18], a 3× suppression of g_{m3} is achieved by an optimum choice of six metals for $S = 1$. It was found that, the optimized results benefit from the consideration of FLP. Notably, a 3.2× and 3.4× reduction in g_{m3} is achieved for $S = 0.70$ and 0.43 respectively (Fig. 4(d–f)) using only four metals (W-19.5%, Ru-14.9%, Ni-30.2%, Au-35.4% for $S = 0.70$, and W-18.7%, Ru-13.8%, Ni-23.7% Au-43.8% for $S = 0.43$). To explain, the metals chosen have work-functions which are relatively far apart, but FLP allows the g_{m3} curves to fall within a narrow optimization window. Thus, considering finite FLP leads to a

better g_{m3} compensation which eventually results in a better optimization with a smaller number of metals. The I_D-V_{GS} of the conventional and MMG HEMTs are shown in Fig. 4(g). Higher sub-threshold slope (SS) and higher off-state current are (one order of magnitude) observed for MMG HEMTs. The higher SS suggests a slower turn-on of the MMG HEMTs. A slower turn-on of the transistor (near $V_{GS} \approx V_{TH}$, which corresponds to the quiescent bias point in deep class AB operation) is highly desired to improve the linearity of highly efficient deep class AB amplifiers [32]. In MMG HEMT, as SS reaches approximately 1.6 times its initial value, the peak of g_{m3} is subsequently reduced by a factor of 3. The increased SS also causes a slight decrease in the peak value of g_m, reducing it by 6% in MMG HEMTs, as shown in Fig. 4(h). These findings indicate a limit to the suppression of the g_{m3} peak value.

Nevertheless, it may seem that a greater extent of FLP would result in better g_{m3} suppression and enhanced linearity, which is not the case. In fact, a complete pinning of the fermi level (S=0) corresponds to the conventional device case of a single metal (without any threshold variation). In this work, S values reported in the literature for experimental cases were considered.

C. Large-Signal Simulation

After the device-level engineering of MMG, compact models of the devices are done using MIT Virtual Source GaN-HEMT (MVSG) model [33]. Results of single tone load pull simulation at 5 GHz are illustrated in Fig. 5. The total gate width is chosen as 100 μm for each transistor. The transistors were biased at deep class AB (high efficiency, highly nonlinear region) with $I_{D,Q}$ = 50 mA/mm. Fig. 5(a) shows that, the fundamental output power ($P_{out,fund}$) is identical for all cases (conventional and MMG HEMT with three FLP factors).

The PA gain of the MMG HEMT is more linear than a conventional HEMT (P_{1dB} = 0.59 W/mm, 3.64 W/mm for conventional HEMT and MMG (S = 0.43) HEMT respectively) for a longer portion of input RF power, as depicted in Fig. 5(b). Although at low output powers, the gain in MMG HEMTs is lower by an insignificant amount, we ought to focus on the high output power region ($P_{out} \approx$ 22dBm) since PAs are required to operate at higher P_{out}. The gain compression of the PAs suggest better linearity performance of the MMG HEMTs as shown in Fig. 5(c). Soft compression of the PAs are minimized in MMG HEMTs. Gain compression for MMG HEMT ($S = 0.43$) is nearly zero until P_{out} = 24 dBm (2.52 W/mm), a quality highly desirable by high power, high efficiency PAs.

Two-tone load-pull simulation was conducted to evaluate RF linearity. The center frequency was set at 5 GHz with a frequency spacing of 10 MHz. A power sweep to find out $OIP3$ and $OIP3/P_{DC}$ are shown in Fig. 6(a)–(b). The dc quiescent bias point was chosen at $V_{DS,Q}$ = 28 V, $I_{D,Q}$ = 50 mA/mm. MMG HEMTs show considerably higher $OIP3$ and $OIP3/P_{DC}$.

Again, both PAs were biased at $V_{DS,Q}$ = 28 V and $I_{D,Q}$ = {50, 73, 90, 105} mA/mm – all four corresponding to deep

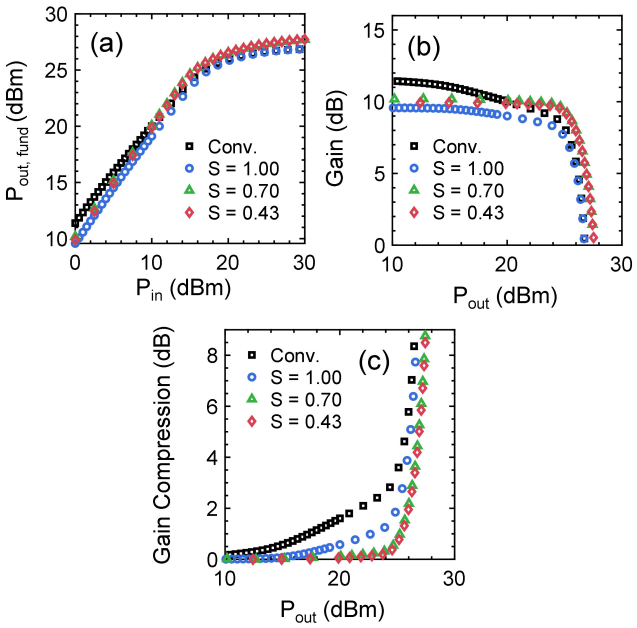

Fig. 5. Single tone large signal simulation of the proposed and conventional AlGaN/GaN HEMTs, showing (a) Fundamental output power, $P_{out,fund}$ (b) PA Gain and (c) Gain compression *vs.* Output power, P_{out}. A flatter gain (with delayed gain compression) than in the conventional case is achieved through the MMG architecture. The transistors are biased at deep class AB with $V_{DS,Q}$ = 28 V, $I_{D,Q}$ = 50 mA/mm and f = 5 GHz. In this work, the total gate width is 100 μm for each transistor.

class AB operation and the linearity metrics were extracted at P_{out} = 15 dBm. The sweet spot for MMG HEMT shifts to lower $I_{D,Q}$ (50 mA/mm, deeper class AB) with S = 0.43 when compared to no pinning considered (mid-level $I_{D,Q}$ = 73 mA/mm). The improvement in $OIP3$ is eventually better in case of pinning factor S = 0.43, supporting the device level optimization achieved (Fig. 6(c)). Improvement in $OIP3$ is 2.2 dB, 7.9 dB and 10.7 dB for S = 1, 0.70 and 0.43 respectively compared to conventional HEMT, at $I_{D,Q}$ = 50 mA/mm. $OIP3/P_{DC}$ is found the highest (18.9 dB) for S = 0.43, as shown in Fig. 6(d).

In GaN HEMT PAs, to maintain a desired level of $IMD3$, OBO is a system-level requirement for PA operation, at the expense of PAE [34]. This simulation demonstrates that the required $IMD3$ can be obtained at lower OBO, even when FLP is included in the simulation framework. Fig. 7(a) shows the achieved $IMD3$ at three levels of OBO. After considering practical FLP, a lower $IMD3$ value can be achieved, manifesting the viability of highly linear operation of the MMG HEMT (13.9 dB lower than conventional HEMT at 6 dB OBO with S = 0.43). The PAE *vs.* OBO trend demonstrated in Fig. 7(b) confirms that, PAE is not compromised for linear operation of PAs (37.2 % for MMG (S = 0.43), 31.4% for conventional HEMT, at 6 dB OBO). At 6 dB OBO, a consequent lower $IMD3$ and higher PAE relieve the linearity-efficiency trade-off. To better illustrate, Fig. 7(c) plots PAE values *vs.* $IMD3$. With $IMD3$ decreasing, PAE eventually drops. However the PAE drop is delayed in MMG HEMTs. At −40 dBc $IMD3$, the PAE values are 6.66%, 14.28%, 31% and 37% for conventional HEMT, MMG HEMT with S = 1.00, 0.70 and 0.43 respectively.

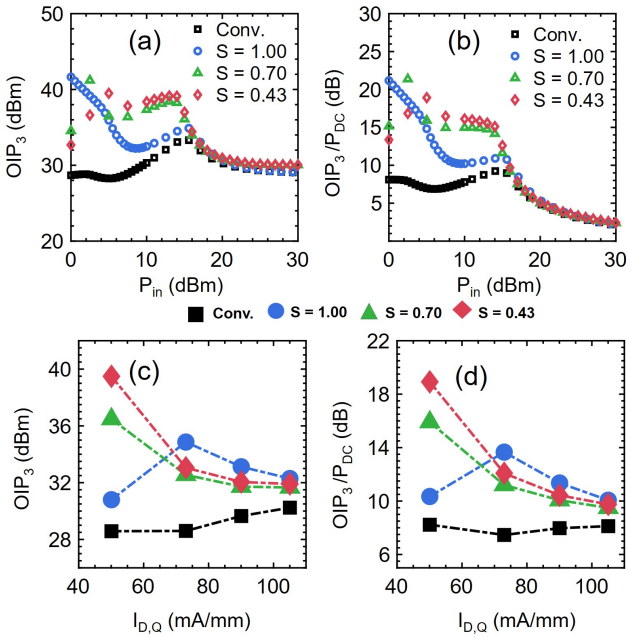

Fig. 6. (a) OIP_3 and (b) OIP_3/P_{DC} *vs.* input power, P_{in}, extracted at $I_{D,Q}$ = 50 mA/mm and $V_{DS,Q}$ = 28 V. (c) OIP_3 (d) OIP_3/P_{DC} at different current bias conditions show that MMG HEMT outperforms conventional HEMT at three FLP factors. The data are extracted at P_{out} = 15 dBm output power.

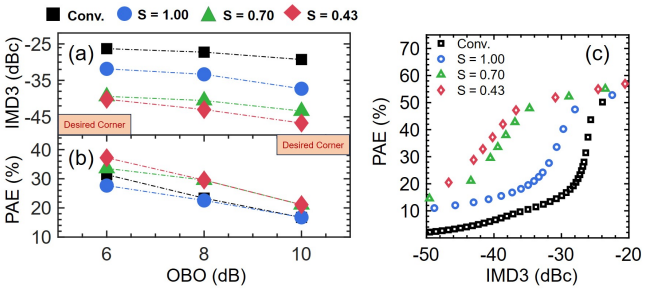

Fig. 7. (a) Improved (suppressed) *IMD3* achieved for MMG (for all finite FLPs) at lower OBO suggesting its viability as an effective device to operate close to P_{sat}. (b) PAE at different output power-back-off (OBO) for conventional HEMT and MMG HEMTs, considering three FLP factors. (c) *IMD3 vs.* PAE. At a certain *IMD3*, MMG HEMTs provide higher PAE, alleviating the linearity-efficiency trade-off. ($V_{DS,Q}$ = 28 V, $I_{D,Q}$ = 50 mA/mm)

In a bar plot, Fig. 8 shows delayed gain compression for the three cases of MMG HEMT, validating MMG HEMT's capability to operate linearly at higher output powers. Though P_{sat} value is 1.6 W/mm lower in MMG (Fig. 8) with strong FLP (S = 0.43) than conventional HEMT, a high-power linear operation is only feasible in MMG.

D. Modulated Signal Simulation

Modulated signal simulations were done using a series of 5G FR1 signals. System level FOMs such as adjacent channel power ratio (ACPR) and error vector magnitude (EVM) were recorded at 5 GHz.

The output power spectral density (PSD) of the PAs are depicted in Fig. 9, evaluated at P_{out} = 20 dBm. With a signal bandwidth of 100 MHz, the MMG HEMT shows robustness

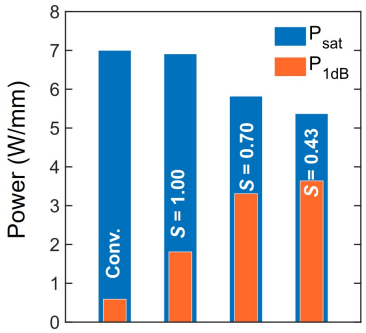

Fig. 8. Impact of FLP on output referred 1-dB compression point (P_{1-dB}) and P_{sat}. Conv. represents the conventional HEMT. The rest of the three cases correspond to MMG HEMT with three different FLP factors. The results reflect MMG HEMT's capability to operate linearly at higher output power.

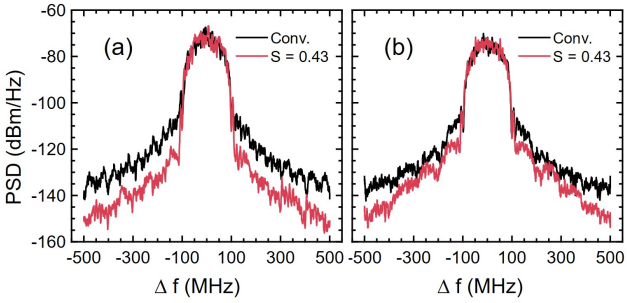

Fig. 9. Power spectral density (PSD) of conventional and MMG (S = 0.43) HEMTs at 5 GHz, (P_{out} = 20 dBm, Bandwidth = 100 MHz) (a) 16-QAM OFDM and (b) 64-QAM OFDM signals.

in substantially reducing the side-lobes at 16-QAM (Fig. 9(a)) and 64-QAM (Fig. 9(b)) OFDM signals.

The constellation diagrams for 16-QAM OFDM signal are shown in Fig. 10. A comparison between the PAs' constellation diagram illustrates that MMG HEMT's distortion is less, due to more linear nature of the PA.

Fig. 11 shows ACPR and EVM at different output power levels under 100 MHz 16-/64-QAM modulated signals (0.4/0.6 Gb/s). MMG HEMTs achieved better than −40 dBc upto P_{out} = 20 dBm for both 16-/64-QAM OFDM signals (Fig. 11(a–b)). Evaluated at P_{out} = 20 dBm, MMG HEMT (S = 0.43) exhibits 2% and 2.6% lower value of EVM for 16-/64-QAM OFDM signals, compared to baseline case (Fig. 11(c–d)).

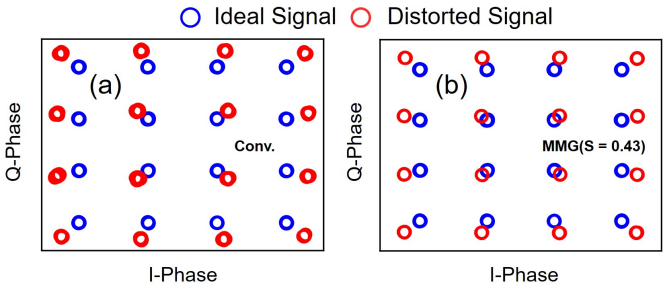

Fig. 10. Constellation diagram for (a) Conventional and (b) MMG HEMT (S = 0.43) at 5 GHz under 100 MHz 16-QAM OFDM signal.

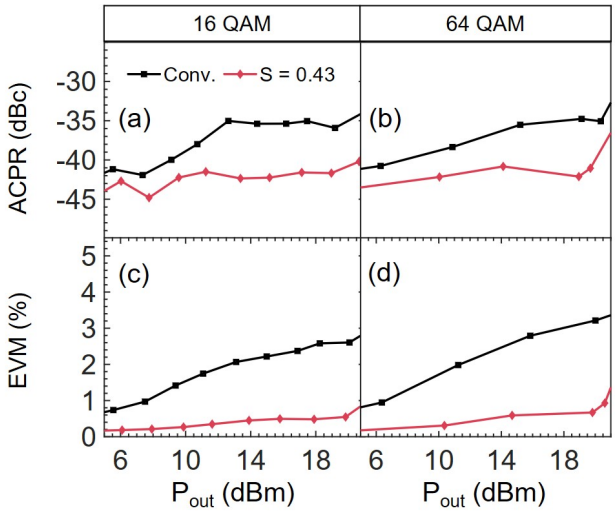

Fig. 11. Modulated Signal performance of the conventional and proposed MMG HEMTs at 5 GHz with different 5G FR1 signals. ACPR *vs.* P_{out} at 100 MHz (a) 16 QAM OFDM (0.4 Gb/s) (b) 64 QAM OFDM (0.6 Gb/s). EVM *vs.* P_{out} at 100 MHz (c) 16-QAM OFDM (0.4 Gb/s) (d) 64-QAM OFDM (0.6 Gb/s).

IV. Conclusion

The MMG architecture effectively enhances GaN HEMT linearity by modulating V_{TH} to suppress g_{m3}. Two different approaches to implement MMG HEMT are proposed : different gate metals along the width of the finger, and different metals in different fingers. Effect of FLP is considered in the MMG architecture. A maximum of 3.4× reduction in g_{m3} was achieved after optimization. This in turn, resulted in 10.7 dB improvement in $OIP3/P_{DC}$ compared to conventional HEMT, in deep class AB operation. MMG HEMT exhibits $P_{1\text{-}dB}$ of 25.6 dBm (3.6 W/mm), 7.9 dB (3 W/mm) higher than conventional HEMT. Furthermore, distortion due to PA in modulated signals is shown to be reduced. ACPR is maintained below -40 dBc upto $P_{out} = 20$ dBm. EVM is reduced by 2.6% in MMG architecture at 5 GHz, under a 100 MHz 64-QAM OFDM signal. More broadly, this study links device-level and system-level performance metrics, demonstrating that the suppression of g_{m3} results in improved PA performance.

References

[1] K. Hoo Teo, Y. Zhang, N. Chowdhury, S. Rakheja, R. Ma, Q. Xie, E. Yagyu, K. Yamanaka, K. Li, and T. Palacios, "Emerging gan technologies for power, rf, digital, and quantum computing applications: Recent advances and prospects," *Journal of Applied Physics*, vol. 130, no. 16, 2021.

[2] U. K. Mishra, L. Shen, T. E. Kazior, and Y.-F. Wu, "GaN-Based RF Power Devices and Amplifiers," *Proceedings of the IEEE*, vol. 96, no. 2, pp. 287–305, 2008.

[3] H. W. Then, S. Dasgupta, M. Radosavljevic, P. Agababov, I. Ban, R. Bristol, M. Chandhok, S. Chouksey, B. Holybee, C. Huang *et al.*, "3d heterogeneous integration of high performance high-k metal gate gan nmos and si pmos transistors on 300mm high-resistivity si substrate for energy-efficient and compact power delivery, rf (5g and beyond) and soc applications," in *2019 IEEE International Electron Devices Meeting (IEDM)*. IEEE, 2019, pp. 17–3.

[4] Y.-F. Wu, A. Saxler, M. Moore, R. Smith, S. Sheppard, P. Chavarkar, T. Wisleder, U. Mishra, and P. Parikh, "30-W/mm GaN HEMTs by Field Plate Optimization," *IEEE Electron Device Letters*, vol. 25, no. 3, pp. 117–119, 2004.

[5] Y.-F. Wu, M. Moore, A. Saxler, T. Wisleder, and P. Parikh, "40-W/mm Double Field-plated GaN HEMTs," in *2006 64th device research conference*. IEEE, 2006, pp. 151–152.

[6] T. Palacios, A. Chakraborty, S. Rajan, C. Poblenz, S. Keller, S. DenBaars, J. Speck, and U. Mishra, "High-Power AlGaN/GaN HEMTs for Ka-Band Applications," *IEEE Electron device letters*, vol. 26, no. 11, pp. 781–783, 2005.

[7] W. Li, B. Romanczyk, M. Guidry, E. Akso, N. Hatui, C. Wurm, W. Liu, P. Shrestha, H. Collins, C. Clymore, S. Keller, and U. K. Mishra, "Record RF Power Performance at 94 GHz From Millimeter-Wave N-Polar GaN-on-Sapphire Deep-Recess HEMTs," *IEEE Transactions on Electron Devices*, pp. 1–6, 2023. doi: 10.1109/TED.2023.3240683

[8] "Power Amplifiers Performance Survey 2000-Present, author=Wang, Hua and Wang, Fei and Nguyen, Huy Thong and Li, Sensen and Huang, Tzu-Yuan and Ahmed, Amr S and Smith, Michael Edward Duffy and Mannem, Naga Sasikanth and Lee, Jeongseok, journal=PA_survey. html, year=2020."

[9] R. ElKashlan, A. Khaled, R. Rodriguez, V. Putcha, U. Peralagu, A. Alian, N. Collaert, P. Wambacq, and B. Parvais, "Linearity Assessment of GaN HEMTs on Si using Nonlinear Characterisation," in *2021 16th European Microwave Integrated Circuits Conference (EuMIC)*. IEEE, 2022, pp. 30–33.

[10] P. Gjurovski, R. Negra, E. Richard, and V. Valenta, "Nonlinear Capacitance Compensation Technique in a Linearity-Enhanced and Broadband GaN PA MMIC for Ku-/K-Band Applications," *IEEE Transactions on Microwave Theory and Techniques*, vol. 71, no. 7, pp. 2958–2969, 2023.

[11] R. Gerzaguet, N. Bartzoudis, L. G. Baltar, V. Berg, J.-B. Doré, D. Kténas, O. Font-Bach, X. Mestre, M. Payaró, M. Färber *et al.*, "The 5G candidate waveform race: a comparison of complexity and performance," *EURASIP Journal on Wireless Communications and Networking*, vol. 2017, pp. 1–14, 2017.

[12] S. H. Sohel, M. W. Rahman, A. Xie, E. Beam, Y. Cui, M. Kruzich, H. Xue, T. Razzak, S. Bajaj, Y. Cao *et al.*, "Linearity Improvement With AlGaN Polarization-Graded Field Effect Transistors With Low Pressure Chemical Vapor Deposition Grown SiNx Passivation," *IEEE Electron Device Letters*, vol. 41, no. 1, pp. 19–22, 2019.

[13] P. Fay, J.-S. Moon, and S. Rajan, "III-N polarization-graded transistors for millimeter-wave applications— Understanding and future potential," *Applied Physics Letters*, vol. 121, no. 14, 2022.

[14] J. Chang, S. Afroz, K. Nagamatsu, K. Frey, S. Saluru, J. Merkel, S. Taylor, E. Stewart, S. Gupta, and R. Howell, "The Super-Lattice Castellated Field-Effect Transistor: A High-Power, High-Performance RF Amplifier," *IEEE Electron Device Letters*, vol. 40, no. 7, pp. 1048–1051, 2019.

[15] Q. Yu, C. Shi, L. Yang, H. Lu, M. Zhang, M. Wu, B. Hou, F. Jia, F. Guo, X. Ma *et al.*, "High Current and Linearity AlGaN/GaN/-Graded-AlGaN:Si-doped/GaN Heterostructure for Low Voltage Power Amplifier Application," *IEEE Electron Device Letters*, vol. 44, no. 4, pp. 582–585, 2023.

[16] W. Song, Z. Zheng, T. Chen, J. Wei, L. Yuan, and K. J. Chen, "RF Linearity Enhancement of GaN-on-Si HEMTs With a Closely Coupled Double-Channel Structure," *IEEE Electron Device Letters*, vol. 42, no. 8, pp. 1116–1119, 2021. doi: 10.1109/LED.2021.3087785

[17] S. Joglekar, U. Radhakrishna, D. Piedra, D. Antoniadis, and T. Palacios, "Large Signal Linearity Enhancement of AlGaN/GaN High Electron Mobility Transistors by Device-level V_T Engineering for Transconductance Compensation," in *2017 IEEE International Electron Devices Meeting (IEDM)*. IEEE, 2017. doi: 10.1109/IEDM.2017.8268457 pp. 25–3.

[18] M. T. Azad, T. Hossain, B. Sikder, Q. Xie, M. Yuan, E. Yagyu, K. H. Teo, T. Palacios, and N. Chowdhury, "AlGaN/GaN based Multi-Metal Gated High Electron Mobility Transistor with Improved Linearity ," *IEEE Transactions on Electron Devices*, 2023.

[19] F. Zhang, X. Zheng, H. Zhang, M. Mi, Y. He, M. Du, X. Ma, and Y. Hao, "Linearity Enhancement of AlGaN/GaN HEMTs With Selective-Area Charge Implantation," *IEEE Electron Device Letters*, vol. 43, no. 11, pp. 1838–1841, Nov 2022. doi: 10.1109/LED.2022.3208121

[20] O. Odabaşı, D. Yılmaz, E. Aras, K. E. Asan, S. Zafar, B. Ç. Akoğlu, B. Bütün, and E. Özbay, "AlGaN/GaN-Based Laterally Gated High-Electron-Mobility Transistors With Optimized Linearity," *IEEE Transactions on Electron Devices*, vol. 68, no. 3, pp. 1016–1023, 2021. doi: 10.1109/TED.2021.3053221

[21] S. Wu, X. Ma, L. Yang, M. Mi, M. Zhang, M. Wu, Y. Lu, H. Zhang, C. Yi, and Y. Hao, "A Millimeter-Wave AlGaN/GaN HEMT Fabricated With Transitional-Recessed-Gate Technology for High-Gain and High-Linearity Applications," *IEEE Electron Device Letters*, vol. 40, no. 6, pp. 846–849, 2019. doi: 10.1109/LED.2019.2909770

[22] J.-S. Moon, B. Grabar, M. Antcliffe, J. Wong, C. Dao, P. Chen, E. Arkun, I. Khalaf, A. Corrion, J. Chappell *et al.*, "High-speed Graded-channel

GaN HEMTs with Linearity and Efficiency," in *2020 IEEE/MTT-S International Microwave Symposium (IMS)*. IEEE, 2020, pp. 573–575.

[23] P. Wang, M. Mi, S. An, X. Du, Y. Zhou, C. Gong, Y. Chen, Q. Zhu, M. Zhang, J. Zhou *et al.*, "Evaluation of Power and Linearity at 30 GHz in AlGaN/GaN HEMT Fabricated by Integrating Transistors With Multiple Threshold Voltages," *IEEE Transactions on Electron Devices*, vol. 71, no. 3, pp. 1421–1427, 2024.

[24] V. Bermudez, "Simple interpretation of metal/wurtzite–GaN barrier heights," *Journal of Applied Physics*, vol. 86, no. 2, pp. 1170–1171, 1999. doi: 10.1063/1.370861

[25] T. Hossain, B. Sikder, M. T. Azad, Q. Xie, M. Yuan, E. Yagyu, K. H. Teo, T. Palacios, and N. Chowdhury, "Fermi-Level Pinning Effect in Gate Region: A Case Study of Multimetal Gated AlGaN/GaN HEMT for High RF Linearity," in *2024 8th IEEE Electron Devices Technology & Manufacturing Conference (EDTM)*. IEEE, 2024, pp. 1–3.

[26] Y. Zhang, K. Wei, S. Huang, X. Wang, Y. Zheng, G. Liu, X. Chen, Y. Li, and X. Liu, "High-Temperature-Recessed Millimeter-Wave AlGaN/GaN HEMTs With 42.8% Power-Added-Efficiency at 35 GHz," *IEEE Electron Device Letters*, vol. 39, no. 5, pp. 727–730, 2018.

[27] Q. Xie, M. Yuan, J. Niroula, B. Sikder, S. Luo, K. Fu, N. S. Rajput, A. B. Pranta, P. Yadav, Y. Zhao *et al.*, "Towards DTCO in High temperature GaN-on-Si Technology: Arithmetic Logic Unit at 300° C and CAD Framework up to 500° C," in *2023 IEEE Symposium on VLSI Technology and Circuits (VLSI Technology and Circuits)*. IEEE, 2023, pp. 1–2.

[28] N. Chowdhury, J. Jung, Q. Xie, M. Yuan, K. Cheng, and T. Palacios, "Performance Estimation of GaN CMOS Technology," in *2021 Device Research Conference (DRC)*. IEEE, 2021, pp. 1–2.

[29] G. Fisichella, G. Greco, F. Roccaforte, and F. Giannazzo, "Current transport in graphene/AlGaN/GaN vertical heterostructures probed at nanoscale," *Nanoscale*, vol. 6, no. 15, pp. 8671–8680, 2014.

[30] H. B. Michaelson, "The work function of the elements and its periodicity," *Journal of applied physics*, vol. 48, no. 11, pp. 4729–4733, 1977.

[31] B. Ofuonye, J. Lee, M. Yan, C. Sun, J.-M. Zuo, and I. Adesida, "Electrical and microstructural properties of thermally annealed Ni/Au and Ni/Pt/Au Schottky contacts on AlGaN/GaN heterostructures," *Semiconductor Science and Technology*, vol. 29, no. 9, p. 095005, 2014. doi: 10.1088/0268-1242/29/9/095005

[32] H. Lu, B. Hou, L. Yang, X. Niu, Z. Si, M. Zhang, M. Wu, M. Mi, Q. Zhu, K. Cheng *et al.*, "AlN/GaN/InGaN Coupling-Channel HEMTs for Improved g_m and Gain Linearity," *IEEE Transactions on Electron Devices*, vol. 68, no. 7, pp. 3308–3313, 2021. doi: 10.1109/TED.2021.3082104

[33] R. Fang, D. Ma, U. Radhakrishna, and L. Wei, "MVSG GaN-HEMT Model: Approach to Simulate Fringing Field Capacitances, Gate Current De-biasing, and Charge Trapping Effects," in *2022 IEEE BiCMOS and Compound Semiconductor Integrated Circuits and Technology Symposium (BCICTS)*. IEEE, 2022, pp. 21–24.

[34] K. Nakatani, Y. Yamaguchi, Y. Komatsuzaki, S. Sakata, S. Shinjo, and K. Yamanaka, "A Ka-Band High Efficiency Doherty Power Amplifier MMIC using GaN-HEMT for 5G Application," in *2018 IEEE MTT-S International Microwave Workshop Series on 5G Hardware and System Technologies (IMWS-5G)*. IEEE, 2018, pp. 1–3.